Journal of Colloid and Interface Science 567 (2020) 339–346

Contents lists available at ScienceDirect

Journal of Colloid and Interface Science

journal homepage: www.elsevier.com/locate/jcis

Dissolution reconstruction of electron-transfer enhanced hierarchical NiS_x-MoO_2 nanosponges as a promising industrialized hydrogen evolution catalyst beyond Pt/C

Benzhi Wang [a], Hexiu Huang [a], Tingting Sun [a], Puxuan Yan [a], Tayirjan Taylor Isimjan [b,*], Jianniao Tian [a], Xiulin Yang [a,*]

[a] Guangxi Key Laboratory of Low Carbon Energy Materials, School of Chemistry and Pharmaceutical Sciences, Guangxi Normal University, Guilin 541004, China
[b] Saudi Arabia Basic Industries Corporation (SABIC) at King Abdullah University of Science and Technology (KAUST), Thuwal 23955-6900, Saudi Arabia

HIGHLIGHTS

- The NiS_x-MoO_2/CC is fabricated by two-step electrodeposition plus calcination.
- The NiS_x-MoO_2/CC outperforms Pt/C at overpotential over 114 mV for HER.
- The NiS_x-MoO_2/CC surpasses widely used industrial Raney Ni catalyst at 500 mA cm^{-2}.
- The catalyst shows excellent long-term stability with almost no decay.
- The superior performance attributes to the porous structure and electronic effect.

GRAPHICAL ABSTRACT

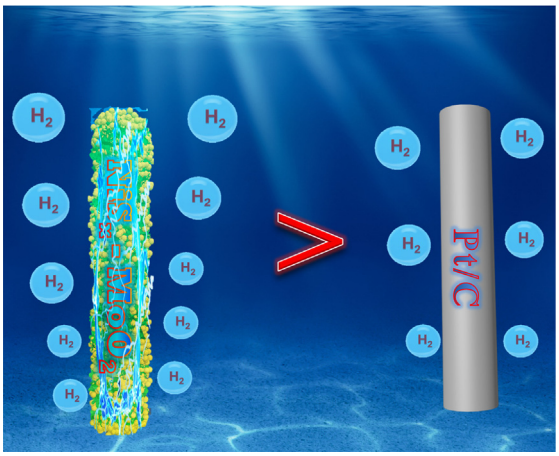

ARTICLE INFO

Article history:
Received 21 December 2019
Revised 2 February 2020
Accepted 9 February 2020
Available online 10 February 2020

Keywords:
NiS_x-MoO_2 nanosponges
Electron transfer
Synergistic effect
Hydrogen evolution
Electrolysis

ABSTRACT

An industrial electro-catalyst obliges three essential features, such as scalability, generating high current density at low overpotential, and long-term stability. Herein, we tackle those challenges using NiS_x-MoO_2 nanosponges on carbon cloth based hydrogen evolution catalyst. The target catalyst was synthesized through a series of simple and scalable methods, including dissolution, reconstruction, and chemical vapor deposition. The optimized NiS_x-MoO_2/CC catalyst exhibits a superior hydrogen evolution catalytic activity far better than commercial Pt/C meanwhile surpasses widely used industrial Raney Ni catalyst by many aspects, namely lower overpotential at 500 mA cm^{-2} current density and smaller Tafel plot in 30 wt% KOH solution. This excellent electrocatalytic activity is attributed to enhanced mass transfer and faster reaction kinetics due to the unique hierarchical porous structures, as well as the synergistic electron transfer effect between the two components of NiS_x and MoO_2 species. This work may provide a new strategy for the design of better hydrogen evolution catalyst for industrial application.

1. Introduction

Hydrogen has been recognized as one of the most promising alternatives to conventional fossil [1,2]. As a clean and efficient

* Corresponding authors.
E-mail addresses: isimjant@sabic.com (T.T. Isimjan), xlyang@gxnu.edu.cn (X. Yang).

https://doi.org/10.1016/j.jcis.2020.02.027
0021-9797/

technology, electrocatalytic water splitting stands out among the in various hydrogen production technologies since it produces high-purity hydrogen with unlimited water resources. Moreover, it can easily be bundled with other renewable energy sources, such as solar wind energy [3]. There are two types of industrial electrolyzers depending on the water pH. However, the alkaline electrolyzer is widely used because of less corrosion and lower capital cost. On the other hand, the acidic electrolyzer generates higher current density [4]. Nevertheless, the price of H_2 generated from water electrolysis is still much higher than that of steam reforming. Therefore, producing scalable, low-cost, durable, and efficient electrode is an important step to reduce the capital cost of electrolyzer subsequently generate cheaper H_2. The hydrogen evolution reaction (HER) that occurred in the cathode is hindered by low conductivity and a lack of active sites. Currently, Pt-based noble metal alloys are by far the most effective catalysts for HER [5]. However; their low reserves and high cost limit their widespread application. Therefore, developing efficient and earth-abundant HER catalysts are highly desirable. At present, the earth-abundant transition metal alloys [6] and their oxides [7,8], nitrides [9,10], sulfides [11], phosphides [12], and selenides [13] have been extensively studied as cathodes catalysts for HER. But, the weak intrinsic activities and poor electrical conductivities limit their HER performances [14]. Furthermore, to satisfy the strict industrial standard, the HER catalyst should be operated at a high current density [15] (>400 mA cm^{-2}) with relatively low overpotential for an extended period. Based on the above considerations, a simple process of fabricating a rationally engineered HER catalyst with excellent conductivity, high active site density as well as the durability at high current density is a critical step to compete with the ongoing industrial process. It is almost impossible to find a single material that can satisfy all those requirements; therefore, designing a hybrid material is necessary.

In recent years, there is an extensive investigation on MoO_2 with a distorted rutile structure due to its metal-like conductivity (1.14×10^4 S at 300 K for bulk materials) and high chemical stability [16]. However, most studies have focused on improving HER performance by building specific nanostructures, which have not worked much on MoO_2-based composites [17,18]. In spite of these advantages, the nanostructured MoO_2 materials are limited by a lack of active sites for HER [19]. On the other hand, Ni-based electrocatalysts have high corrosion resistance in alkaline solution and abundant active sites [20,21]. But, the nickel-based electrocatalysts are mostly in powder form and need to be coated on a conductive substrate for HER application [22,23]. The catalyst coating on the substrate causes a decrease in the catalytic performance of the powder catalyst because of the mechanical shedding. Moreover, the catalyst conductivity may decrease due to the use of polymer binders during the preparation. Furthermore, the catalytic performance of the materials is closely related to their morphology and composition. The sponge-like porous structure provides high surface area, sufficient active site and better mass transfer. Moreover, it also prevents catalyst aggregation [24,25]. To the best of our knowledge, there is no report on the HER application of NiS_x-MoO_2 nanosponges.

Herein, we develop a highly-active NiS_x-MoO_2 nanosponge decorated carbon cloth as HER catalyst (NiS_x-MoO_2/CC). It is the first report of a simple yet industrial compatible strategy based on NiS_x-MoO_2/CC. The synthesis process includes a two-step electrodeposition followed by vulcanization processing (Scheme 1). In this design, we not only combined the unique features of both components such as high conductivity of MoO_2 and high HER activity of NiS_x but also eliminated the coating process by growing NiS_x directly on the surface of MoO_2. The optimized NiS_x-MoO_2/CC catalyst only requires overpotentials of 60 and 149 mV (vs. RHE) to reach 10 and 100 mA cm^{-2} in 1.0 M KOH, respectively. Moreover, it outperforms the Pt/C catalyst when the overpotential is higher than 114 mV. Most importantly, the optimized NiS_x-MoO_2/CC requires much smaller overpotentials to reach large current densities (500 mA cm^{-2}@208 mV and 1000 mA cm^{-2}@230 mV) than the industrial HER catalyst-Raney Ni (500 mA cm^{-2}@300–500 mV) in 30% KOH solution [26-28], suggesting a strong industrial perspective.

2. Experimental

2.1. Materials

Nickel nitrate hexahydrate ($Ni(NO_3)_2{\cdot}6H_2O$, ≥98%), ammonium molybdate tetrahydrate ($H_{24}Mo_7N_6O_{24}{\cdot}4H_2O$), sulfur sublimed (S, 99%). All the reagents were analytical reagent and used without further purification. Commercial Pt/C (20 wt% for platinum) was purchased from Alfa Aesar.

2.2. Electrodeposition of Ni-, Mo- and Ni-Mo-species on carbon cloth

Initially, the carbon cloth (CC, 1 cm × 1.5 cm) was ultrasonically cleaned in sulfuric acid, deionized water, and ethanol for 5 min, respectively, and cycled 3 times to remove impurities. Electrodeposition was performed in a standard three-electrode system, in which the treated CC, graphite plate, and saturated calomel electrode (SCE) were used as working, counter, and reference electrodes, respectively. The Ni-species/CC samples were fabricated by continuous electrodeposition for 1.0 h at −10 mA cm^{-2} in 0.1 M $Ni(NO_3)_2$ solution. These obtained samples were rinsed with a large amount of water and naturally dried for use. Subsequently, the samples of Ni-species/CC were used as working electrodes at −10 mA cm^{-2} for electrodeposition different times from 0.5 to 2.0 h in 0.1 M $H_{24}Mo_7N_6O_{24}$ solution. The resulted samples are nominated as Ni-Mo-species/CC-0.5 h, Ni-Mo-species/CC-1 h and Ni-Mo-species/CC-2 h, respectively. As a control, electrodeposition of Mo-species on fresh CC surface (Mo-species/CC) was also prepared at −10 mA cm^{-2} for 1.0 h in 0.1 M $H_{24}Mo_7N_6O_{24}$ solution.

2.3. Synthesis of NiS_2/CC, MoO_2/CC and NiS_x-MoO_2/CC

The catalyst of NiS_x-MoO_2/CC was prepared by coating 0.5 g of sulfur powder on a series of Ni-Mo-species/CC surfaces, and slowly heating (3 °C min^{-1}) to a specific temperature (400, 500 or 600 °C) for 4.0 h in Ar atmosphere (20 sccm), and then cooling down to room temperature. After sufficient water washing and drying, the prepared materials were nominated as NiS_x-MoO_2/CC (from XRD data). As a comparison, the NiS_2/CC and MoO_2/CC were also prepared by a similar method as mentioned above.

2.4. Characterization

Scanning electron microscopy (SEM, Quanta FEG 200, Holland) and transmission electron microscopy (TEM, JEOL, JEM-2100F) were used to investigate the morphologies and microstructures of the designed materials. X-ray powder diffraction (XRD) data was detected by a D/Max 2500 V PC with Cu Kαradiation from Rigaku. The chemical states of the samples were examined by X-ray photoelectron spectroscopy (XPS, model: JPS-9010 TR Photoelectron Spectrometer, Japan). Raman spectroscopy was acquired from an inVia confocal Raman microscope (Renishaw, England).

2.5. Electrochemical measurements

The electrochemical performance of the as-prepared catalysts were studied by an electrochemical workstation of Biologic

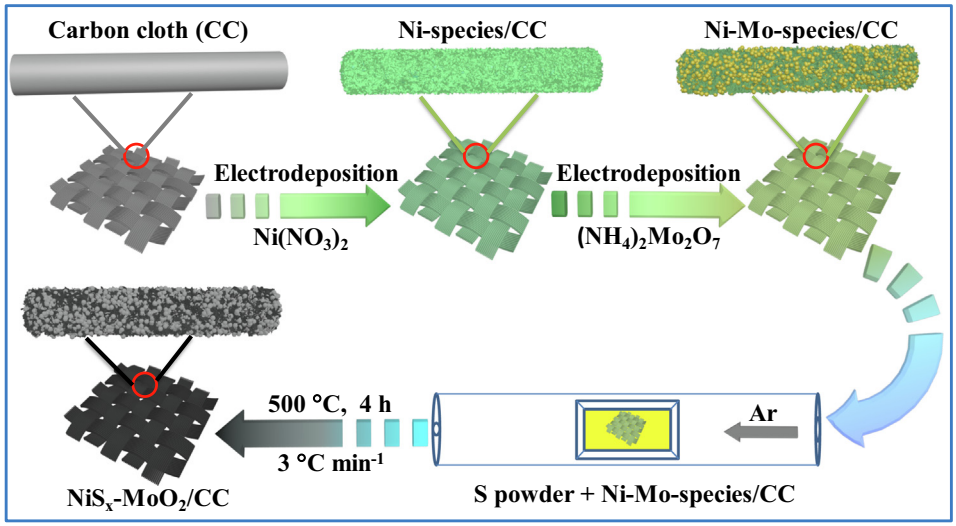

Scheme 1. Schematic diagram of the formation of NiS_x-MoO_2/CC catalyst.

VMP3 with a typical three-electrode system in 1.0 M KOH electrolyte. The catalysts modified carbon cloth, graphite plate and SCE were used as working, counter and reference electrodes, respectively. Cyclic voltammetry (CV) tests were firstly carried out for about 5 cycles to stabilize the electrocatalytic performance of the catalyst at a scan rate of 20 mV s^{-1}. Then, liner sweep voltammetry (LSV) curves were performed at a low scan rate of 0.5 mV s^{-1}, and electrochemical impedance spectroscopy (EIS) was evaluated near the onset potential in the frequency range from 200 kHz to 10 mHz. All potentials (vs. SCE) in this work were calibrated to the RHE by the average CV curves of the two potentials at which the current crossed zero (1.040 V) was taken to be the thermodynamic potential in H_2-saturated 1.0 M KOH (Fig. S1). The overall water splitting was measured in 30 wt% KOH solution with a scan rate of 5 mV s^{-1}. All reported curves had been corrected by *i*R compensation and all the electrochemical tests were performed at room temperature (25 ± 1 °C).

3. Results and discussion

The X-ray diffraction (XRD) patterns are used to investigate the crystal structures of the optimized NiS_x-MoO_2/CC as well as NiS_x/CC, MoO_2/CC and Ni-Mo-species/CC initially. As shown in Fig. 1a, the diffraction peaks of the NiS_x-MoO_2/CC material are substantially consistent with the standard diffraction patterns of MoO_2 (JCPDS: 76-1807) [29], NiS (JCPDS: 75-0613) and NiS_2 (JCPDS: 89-1495), respectively. It is noteworthy that no diffraction peaks of MoS_x are observed indicating either low content or amorphous form of MoS_x. As a comparison, the XRD patterns of NiS_x/CC and MoO_2/CC have also been explored, and they are very similar to the disassembly of NiS_x-MoO_2/CC. Note that the precursor of Ni-Mo-species/CC mainly contains $Ni(OH)_2$ (01-1047) and MoO_2 segments (Fig. S2). Raman spectroscopy is used to explore the changes in band structures of the materials. We can observe that the Ni-Mo-species/CC has almost no scattering peaks, while NiS_x/CC has a typical characteristic NiS_2 peak at 476.5 cm^{-1}, which belongs to A_g photons [30]. Notably, the MoO_2/CC presents two types of Raman peaks, seven of which are typical MoO_2 characteristic peaks, and the other two are typical MoS_2 characteristic peaks at 383.6 (in-plane vibration of Mo-S) and 405.1 cm^{-1} (out-plane vibration of S-atoms) [31,32]. Differentially, the NiS_x-MoO_2/CC primarily exhibits two distinct MoS_2 peaks, while all other scattering peaks are very weak, indicating that there is a thin layer of MoS_2 covering on the surface of the composite. The presence of MoS_2 species may help to increase the interaction between MoO_2 and NiS_x species, thereby enhancing electron mobility in the composite [33,34].

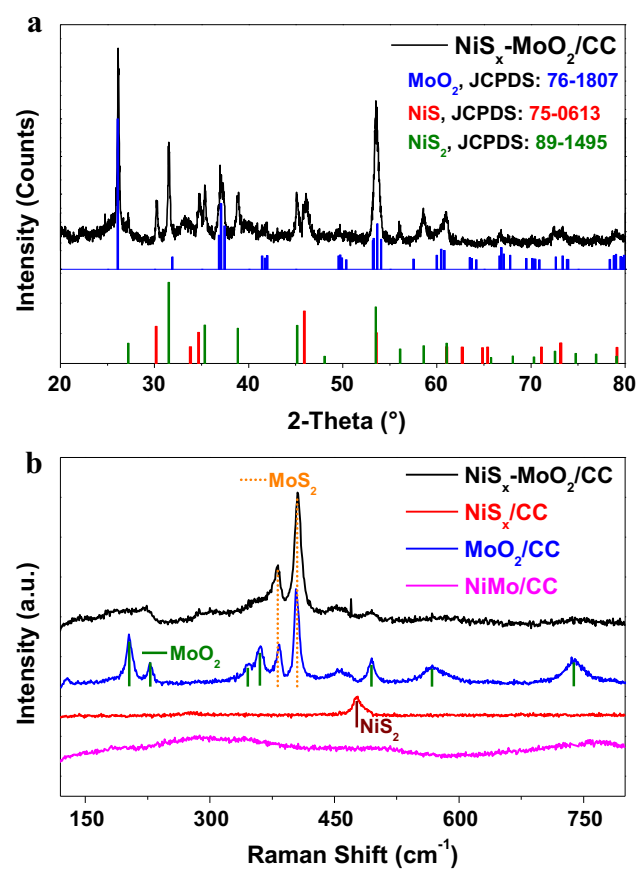

Fig. 1. (a) XRD pattern of the optimized NiS_x-MoO_2/CC and inset histograms of standard MoO_2, NiS and NiS_2. (b) Raman spectra of Ni-Mo-species/CC, NiS_x/CC, MoO_2/CC and NiS_x-MoO_2/CC.

The morphologies and microstructures of the materials are further studied by scanning electron microscopy (SEM) and transmission electron microscopy (TEM). It shows that the rugae-like

Ni-species arrays grow vertically on CC surface and created large holes between the nanosheets (Fig. 2a). After electrodeposited Mo-species, a certain level of porosity is visible on the Ni-Mo composite (Fig. 2b). After vulcanization at 500 °C in Ar atmosphere, some particulate materials appear on the surface of NiS_x-MoO_2/CC (Fig. 2c). Interestingly, the cross-sectional SEM image shows a uniformly nanosponge-like NiS_x-MoO_2 structure (inset of Figs. 2c and S3a). These porous structures not only facilitate mass transfer but also expose more active sites, thereof improve the electrochemical performance. The TEM image shows some flaky and granular structures, which is consistent with the SEM results (Figs. 2d and S3b). High-resolution TEM image shows clear lattice stripes with a lattice spacing of 0.242, 0.283 and 0.198 nm corresponding to the (1 1 1) crystal plane of MoO_2, (2 0 0) plane of NiS_2 and (1 0 2) plane of NiS, respectively (Fig. 2e) [35–37]. Moreover, we have observed the layer stacking characteristics of two-dimensional materials, which belong to the typical MoS_2 species [38]. The high-angle annular dark field (HAADF) TEM elemental mappings reveal that Ni, Mo, S, and O are uniformly distributed in NiS_x-MoO_2/CC (Fig. 2f–g). As comparison, we also present the SEM images of NiS_x-MoO_2/CC catalysts with different deposition times of Mo species (Figs. S3c–f). In addition, the inductively coupled plasma mass spectrometry (ICP-MS) test results showed that the mass fractions of Ni and Mo in the NiS_x-MoO_2/CC composite were 28.1 and 15.1 wt%, respectively. The atomic ratio of Ni /Mo was 3.03/1 (Table S1).

The surface composition and chemical states of NiS_x-MoO_2/CC are further clarified through X-ray photoelectron spectroscopy (XPS). The typical XPS survey spectra in Fig. S4a confirms the existence of Mo, Ni, O, S, and C elements in NiS_x-MoO_2/CC, where the high-resolution C 1s spectrum is convoluted into four peaks at C=C (284.0 eV), C—C (284.8 eV), C—O (286.0 eV) and C=O (288.0 eV) as shown in Fig. S4b [39,40]. The high-resolution Mo 3d spectrum of NiS_x-MoO_2/CC and MoO_2/CC is displayed in Fig. 3a. The XPS peak of NiS_x-MoO_2/CC at 228.6 eV is assigned to Mo $3d_{5/2}$. The corresponding Mo $3d_{5/2}$ peak of NiS_x-MoO_2/CC shows a negative shift by 0.25 eV as compare to that of MoO_2/CC (228.85 eV) [41–43]. Besides, the high-resolution Ni $2p_{3/2}$ region of NiS_x-MoO_2/CC presents two peaks at 853.4 eV and 857.2 eV, accompanied by a strong satellite at 861.8 eV, which represent the two different chemical states of Ni in NiS_x-MoO_2/CC [44,45]. In addition to the same Ni^{2+} and satellite peak positions, the Ni^{4+} species of NiS_x/CC material has a binding energy of 856.3 eV, which results a positive shift of 0.91 eV as compared to that of NiS_x-MoO_2/CC (Fig. 3b). The peaks at 161.4 eV, 162.1 eV and 163.7 eV of S $2p_{3/2}$ are corresponding to S2p of MoS_2, NiS and NiS_2 species, respectively (Fig. 3c) [46]. Moreover, there is a strong peak at 169.1 eV, which can be assigned to S—O species arising from surface oxidation. It should be noted that the slight negative shift on Mo $3d_{5/2}$ (Mo^{4+}) and the significant positive shift on Ni $2p_{3/2}$ (Ni^{4+}) peaks in NiS_x-MoO_2/CC as compare to those of MoO_2/CC and NiS_x/CC. This result indicates that the MoO_2 species have a higher electron density than these of NiS_x species in the composite [47], and the improved electron density can synergistically promote the HER catalytic activity [48].

The HER electrocatalytic activity of NiS_x-MoO_2/CC was firstly optimized by the effect of vulcanization temperatures and electroplating times of Mo-species on the catalytic performance. The results show that the catalyst obtained at vulcanization temperature of 500 °C has the best HER catalytic activity and minimum Tafel slope in 1.0 M KOH solution (Fig. S5). The electrocatalytic activities of the optimized NiS_x-MoO_2/CC catalyst together with MoO_2/CC, NiS_x/CC, NiMo-species/CC and commercial Pt/C (Johnson Matthey, 20 wt% Pt on activated carbon) were further investigated in 1.0 M KOH (Fig. 4a). The HER results reveal that the NiS_x-MoO_2/CC catalyst requires only an overpotential of 60 mV to deliver a geometric current density of −10 mA cm^{-2}, which is similar to Pt/CC (49 mV) and far superior to all other control catalysts as well as most of the previously reported transition metal sulfides catalysts (Table S2). Moreover, the NiS_x-MoO_2/CC and Pt/C catalysts have the same current density (−34.5 mA cm^{-2}) when the overpotential reaches 114 mV. Thereafter, the catalytic activity of

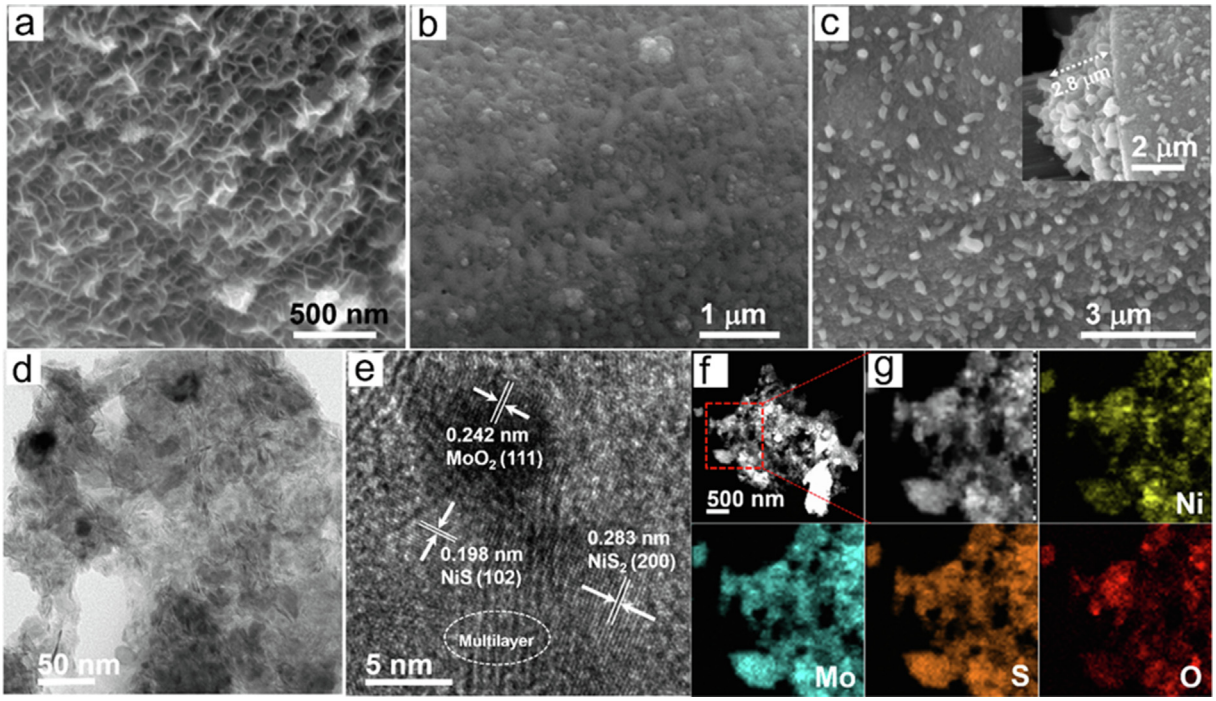

Fig. 2. SEM images of (a) Ni-species/CC, (b) Ni-Mo-species/CC, and (c) NiS_x-MoO_2/CC. (d) TEM image and (e) high-resolution TEM image of NiS_x-MoO_2/CC. (f) HAADF TEM image and (g) enlarge elemental mappings of NiS_x-MoO_2/CC.

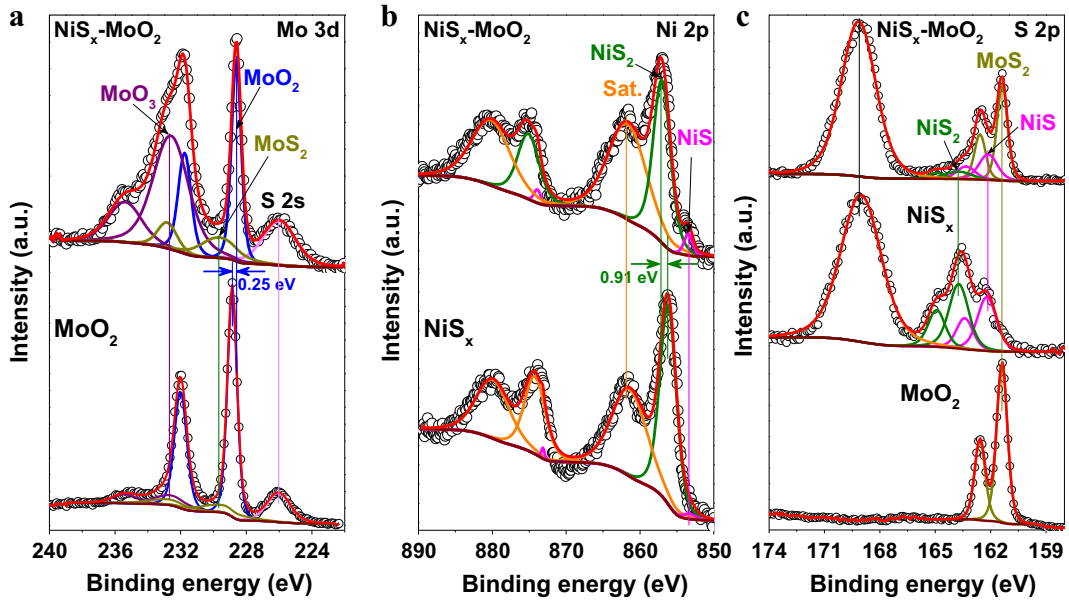

Fig. 3. High-resolution XPS spectra of (a) Mo 3d, (b) Ni 2p and (c) S 2p regions from NiS_x-MoO_2/CC, NiS_x/CC and MoO_2/CC, respectively.

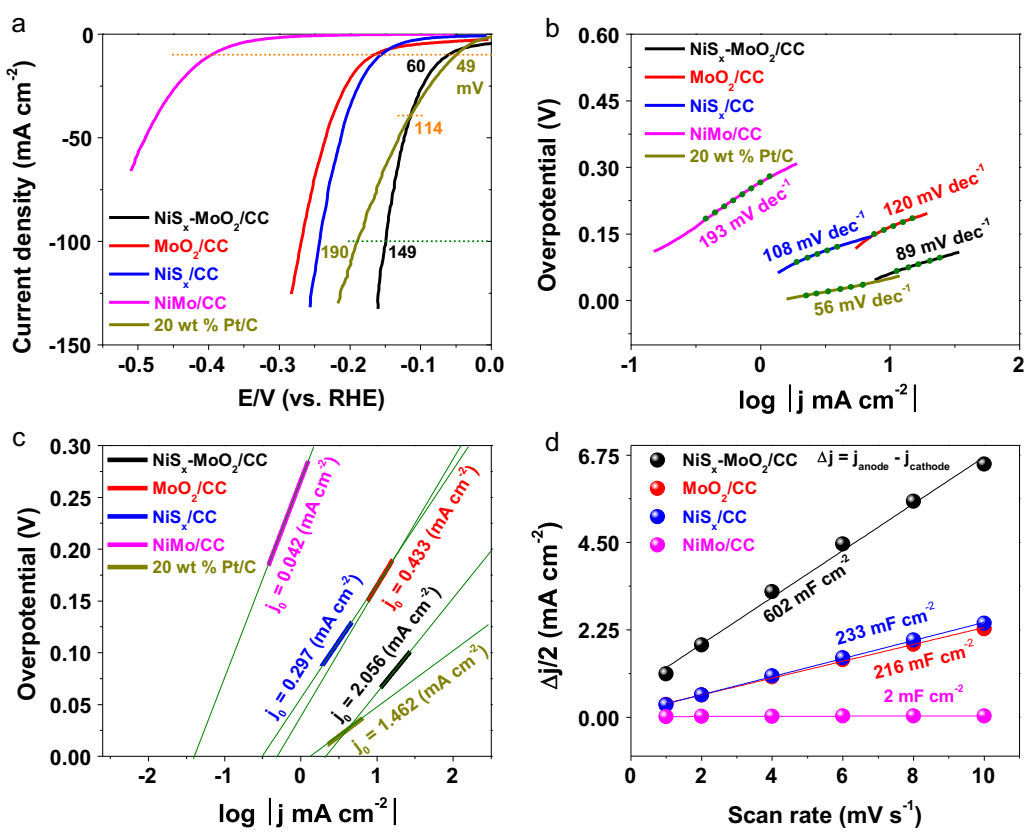

Fig. 4. (a) LSV polarization curves, (b) corresponding Tafel slopes, (c) exchange current density, and (d) summarized double layer capacitance (C_{dl}) of NiS_x-MoO_2/CC, MoO_2/CC, NiS_x/CC, NiMo-species/CC and 20 wt% Pt/C in 1.0 M KOH.

NiS_x-MoO_2/CC is significantly better than that of commercial Pt/C catalyst indicating a great potential for industrial applications because it only requires overpotentials of 208 and 230 mV to reach 500 and 1000 mA cm^{-2} in 30 wt% KOH solution (Fig. S6). The Tafel slope is usually employed to evaluate the reaction kinetics and the rate-determining step during HER process. According to the kinetic modeling results, the Tafel slope values of Volmer, Heyrovsky and Tafel reactions correspond to 120, 40 and 30 mV dec^{-1}, respectively [49]. It is well understood that the hydrogen evolution reaction under alkaline conditions involves two steps [50]. The step 1 is the water dissociation and the intermediates formation (Volmer reaction): $H_2O + M + e^- \rightarrow M\text{-}H_{ad} + OH^-$, followed by either the

desorption step (Heyrovsky reaction): $H_2O + M\text{-}H_{ad} + e^- \rightarrow M + H_2 + OH^-$, or a recombination step (Tafel reaction): $2M\text{-}H_{ad} \rightarrow 2M + H_2$ [51]. As show in Fig. 4b, the Tafel slope of NiS_x-MoO_2/CC is 89 mV dec^{-1}, which is obviously less than that of all control catalysts, indicating a fast Volmer-Heyrovsky mechanism [52]. Moreover, the exchange current density (j_0), the key parameter reflecting the intrinsic activity of HER, was calculated by extrapolation the Tafel slope. As shown in Fig. 4c, the NiS_x-MoO_2/CC exhibited the highest value of 2.056 mA cm^{-2} compared to those of Ni-Mo-species/CC (0.042 mA cm^{-2}), MoO_2/CC (0.433 mA cm^{-2}), NiS_2/CC (0.297 mA cm^{-2}) and Pt/C (1.462 mA cm^{-2}). Meanwhile, the NiS_x-MoO_2/CC also shows the lowest charge transfer resistance (Fig. S7), suggesting the fastest HER kinetics [53].

In general, a better electrocatalytic activity is accompanied by a larger electrochemically active surface area (EASA), and the EASA is normally proportional to the electrochemical double-layer capacitance (C_{dl}). The C_{dl} was calculated by measuring the CV curves in a non-faradaic potential window (Fig. S8). As shown in Fig. 4d, the C_{dl} value of NiS_x-MoO_2/CC is 602 mF cm^{-2}, which is much higher than those of NiS_2/CC (233 mF cm^{-2}), MoO_2/CC (216 mF cm^{-2}) and Ni-Mo-species/CC (2 mF cm^{-2}). The results reveals that the NiS_x-MoO_2 nanosponges with dual active sites generate more accessible active sites in alkaline electrolyte than those of other catalysts, thereby promoting H_2 evolution. At the same time, the turnover frequency (TOF) was adopted to measure the amount of H_2 molecules released per second per active site, which was normally used to evaluate the intrinsic catalytic activity of the catalyst [54]. As show in Fig. S9a, the TOF value increases rapidly as the applied voltage increases in 30 wt% KOH solution. In particular, when the overpotentials are at 150 and 200 mV, the corresponding TOF values are *ca.* 2.8 and 13.7 s^{-1} (Fig. S9b), which are much larger than most reported in the literature [6,55]. It was confirmed that NiS_x-MoO_2/CC has excellent intrinsic catalytic activity.

To satisfy industrial compliance, the optimized HER catalysts coupled with RuO_2 as a counter electrode was tested at high current density in a two-electrode system (Fig. 5a). The steady-state potential polarization curve of the coupled $RuO_2^{(+)}$//NiS_x-$MoO_2^{(-)}$ is show in Fig. 5b. Interestingly, the overall voltage required for total water splitting of the $RuO_2^{(+)}$//NiSx-$MoO_2^{(-)}$ is slightly higher than that of benchmark system of $RuO_2^{(+)}$//Pt/$C^{(-)}$ at a low current density and reaches the same value at 1.74 V (~500 mA cm^{-2}). However, it starts to over the catalytic performance of both $RuO_2^{(+)}$//Pt/$C^{(-)}$ and the existing industrial system (200–400 mA cm^{-2} at 1.8–2.4 V) at high current density (>500 mA cm^{-2}). Besides, it only needs 0.1 V extra voltage for reaching the current density from 500 to 1000 mA cm^{-2}. Furthermore, we gathered some of the high performance the HER catalysts reported in the literatures (Table S3) and compared their results with our optimized catalyst (Fig. 5c). The optimized NiS_x-MoO_2/CC shows the lowest cell voltage for achieving 100 mA cm^{-2} as compared to the rest. Finally, we performed a durability test. As shown in Fig. 5d, the NiS_x-MoO_2/CC catalyst was continuously operated for 120 h in the industrial condition (30 wt% KOH) at a constant current of 500 mA cm^{-2} and almost no degradation was observed indicating a great industrial perspective.

As discussed above, the excellent HER electrocatalytic activity is due to the unique structure of the composite catalyst and the synergistic effect between the two active species. The XPS spectra prove that there is a strong electron transfer effect between MoO_2 and NiSx species, which makes MoO_2 have a partial negative

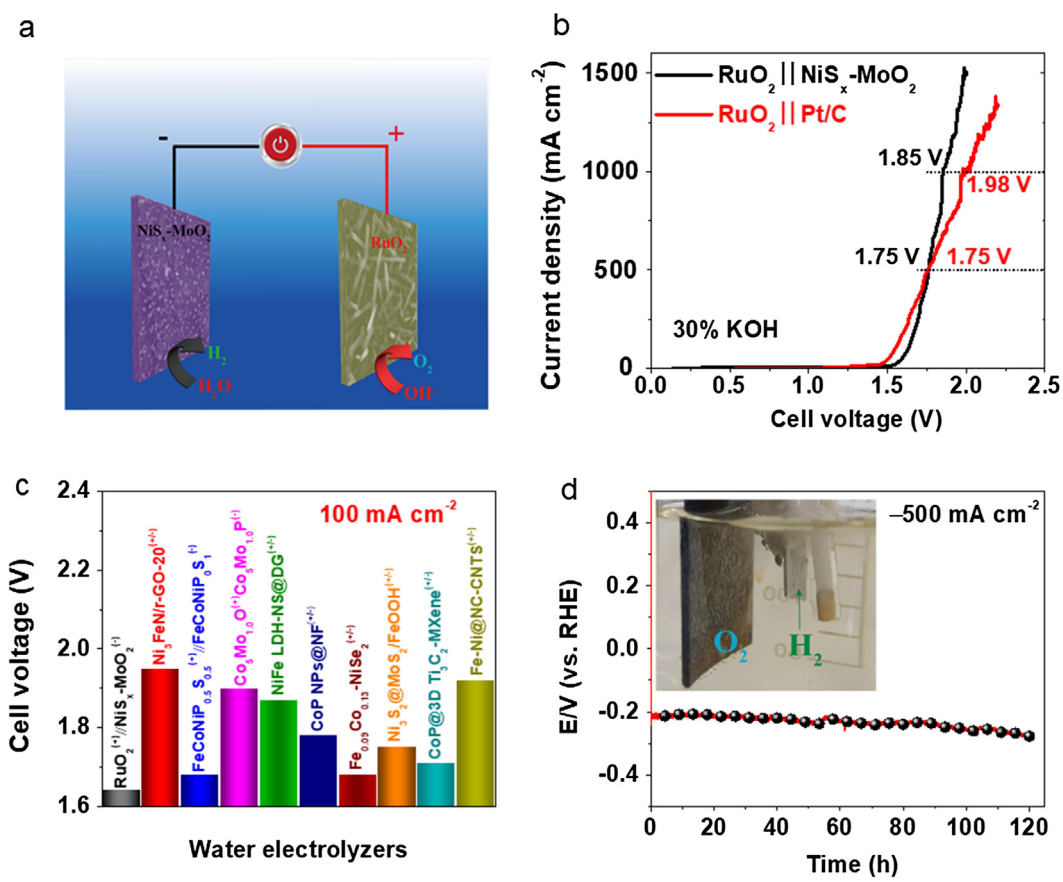

Fig. 5. (a) Schematic diagram of overall-water-splitting electrolytic cell using NiS_x-MoO_2 and RuO_2 as cathode and anode, respectively. (b) Comparison of overall-water-splitting activity of $RuO_2^{(+)}$//NiS_x-$MoO_2^{(-)}$ with noble metal $RuO_2^{(+)}$//Pt/$C^{(-)}$ at high current in 30 wt% KOH. (c) Comparing the cell voltage of the currently available electrolytic cell at 100 mA cm^{-2} in 1.0 M KOH. (d) Durability tests of NiS_x-MoO_2 at −500 mA cm^{-2} in 30 wt% KOH.

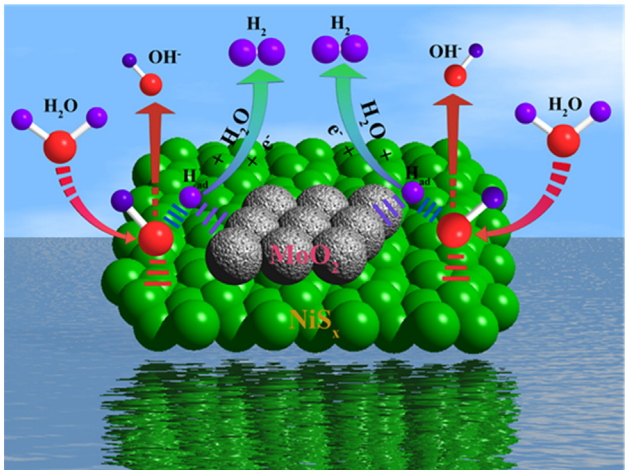

Scheme 2. Schematic diagram of HER catalytic mechanism of NiS_x-MoO_2/CC catalyst in an alkaline solution.

charge, and NiSx takes a somewhat positive charge. In an alkaline environment, the positively charged NiSx species can adsorb H_2O molecules at the interface of the two active sites and synergistically promote the dissociation of H_2O, thereby forming a reactive intermediate of adsorbed hydrogen (M-H_{ad}) on the surface of the MoO_2 species. The formed M-H_{ad} can further bind with one electron and one H_2O molecule, synchronously releasing H_2 through the Heyrovsky step ($M - H_{ad} + e^- + H_2O \rightarrow M + H_2 + OH^-$) (Scheme 2) [51].

4. Conclusion

In summary, we have developed an excellent NiSx-MoO2/CC electrocatalyst using two-step electrodeposition and subsequent vulcanization. The resulted NiSx-MoO2/CC catalyst exhibits superior catalytic activity with a low overpotential of 60 mV at -10 mA cm^{-2}, a small Tafel slope of 89 mV dec^{-1}, a significant exchange current density of 2.065 mA cm^{-2}, and long-term stability in 30 wt% KOH. The excellent results are attributed to the hierarchical porous structures as well as a synergistically catalytic effect for HER between NiSx and MoO2 species. Therefore, the reported method of HER catalyst with unique architecture and enhanced electron transfer effect is also useful for future construction of other high-efficiency materials, such as fuel cells, photocatalysis, lithium-ion batteries, and so on.

CRediT authorship contribution statement

Benzhi Wang: Investigation, Methodology. **Hexiu Huang:** Data curation. **Tingting Sun:** Formal analysis. **Puxuan Yan:** Data curation. **Tayirjan Taylor Isimjan:** Writing - original draft. **Jianniao Tian:** Supervision. **Xiulin Yang:** Writing - review & editing.

Declaration of Competing Interest

The authors declare that they have no known competing financial interests or personal relationships that could have appeared to influence the work reported in this paper.

Acknowledgements

This work has been supported by the National Natural Science Foundation of China (no. 21965005), Natural Science Foundation of Guangxi Province (2018GXNSFAA294077, 2018GXNSFAA281220), Project of High-Level Talents of Guangxi (F-KA18015, 2018ZD004) and Innovation Project of Guangxi Graduate Education (XYCSZ2019056, YCBZ2019031).

Notes

The authors declare no competing financial interest.

Appendix A. Supplementary data

Figs. S1–S9 and Tables S1–S3 give more details on characterization of our synthesized materials and their electrocatalytic performance data; additional XPS and electrocatalytic performance data (PDF). Supplementary data to this article can be found online at https://doi.org/10.1016/j.jcis.2020.02.027.

References

[1] R. Zhang, X. Wang, S. Yu, T. Wen, X. Zhu, F. Yang, X. Sun, X. Wang, W. Hu, Ternary $NiCo_{2-p}X$ nanowires as pH-universal electrocatalysts for highly efficient hydrogen evolution reaction, Adv. Mater. 29 (2017) 1605502.
[2] S. Li, C. Cheng, A. Sagaltchik, P. Pachfule, C. Zhao, A. Thomas, Metal-organic precursor-derived mesoporous carbon spheres with homogeneously distributed molybdenum carbide/nitride nanoparticles for efficient hydrogen evolution in alkaline media, Adv. Funct. Mater. 29 (3) (2019) 1807419.
[3] J. Hao, W. Yang, Z. Peng, C. Zhang, Z. Huang, W. Shi, A nitrogen doping method for CoS_2 electrocatalysts with enhanced water oxidation performance, ACS Catal. 7 (2017) 4214–4220.
[4] K. Pandi, M. Sivakumar, S.-M. Chen, Y.-H. Cheng, T.-W. Chen, A perspective on low-temperature water electrolysis-challenges in alkaline and acidic technology, Int. J. Electrochem. Sci. 13 (2018) 1173–1226.
[5] X. Cheng, Y. Li, L. Zheng, Y. Yan, Y. Zhang, G. Chen, S. Sun, J. Zhang, Highly active, stable oxidized platinum clusters as electrocatalysts for the hydrogen evolution reaction, Energy Environ. Sci. 10 (2017) 2450–2458.
[6] L. Yang, L. Zeng, H. Liu, Y. Deng, Z. Zhou, J. Yu, H. Liu, W. Zhou, Hierarchical microsphere of MoNi porous nanosheets as electrocatalyst and cocatalyst for hydrogen evolution reaction, Appl. Catal., B 249 (2019) 98–105.
[7] R. Sun, Z. Xia, L. Shang, X. Fu, H. Li, S. Wang, G. Sun, Hierarchically ordered arrays with platinum coated PANI nanowires for highly efficient fuel cell electrode, J. Mater. Chem. A 5 (2017) 15260–15265.
[8] Y. Liu, X. Li, W. Bi, M. Jin, An etching-assisted route for fast and large-scale fabrication of non-layered palladium nanosheets, Nanoscale 10 (2018) 7505–7510.
[9] G.-X. Tong, F.-T. Liu, W.-H. Wu, J.-P. Shen, X. Hu, Y. Liang, Polymorphous α- and β-$Ni(OH)_2$ complex architectures: morphological and phasal evolution mechanisms and enhanced catalytic activity as non-enzymatic glucose sensors, CrystEngComm 14 (2012) 5963–5973.
[10] N. Meng, J. Ren, Y. Liu, Y. Huang, T. Petit, B. Zhang, Engineering oxygen-containing and amino groups into two-dimensional atomically-thin porous polymeric carbon nitrogen for enhanced photocatalytic hydrogen production, Energy Environ. Sci. 11 (2018) 566–571.
[11] P. Kuang, T. Tong, K. Fan, J. Yu, In Situ fabrication of Ni–Mo bimetal sulfide hybrid as an efficient electrocatalyst for hydrogen evolution over a wide pH range, ACS Catal. 7 (2017) 6179–6187.
[12] C. Tang, R. Zhang, W. Lu, L. He, X. Jiang, A.M. Asiri, X. Sun, Fe-doped CoP nanoarray: a monolithic multifunctional catalyst for highly efficient hydrogen generation, Adv. Mater. 29 (2017) 1602441.
[13] Y. Guo, Z. Yao, C. Shang, E. Wang, P doped Co_2Mo_3Se nanosheets grown on carbon fiber cloth as an efficient hybrid catalyst for hydrogen evolution, J. Mater. Chem. A 5 (2017) 12043–12047.
[14] B. Ren, D. Li, Q. Jin, H. Cui, C. Wang, Integrated 3D self-supposed Ni decorated MoO2 nanowires as highly efficient electrocatalysts for ultra-highly stable and large-current-density hydrogen evolution, J. Mater. Chem. A 5 (2017) 24453–24461.
[15] P. Millet, S. Grigoriev, Chapter 2 – Water electrolysis technologies, in: L.M. Gandía, G. Arzamendi, P.M. Diéguez (Eds.), Renewable Hydrogen Technologies, Elsevier, Amsterdam, 2013, pp. 19–41.
[16] L. Yang, W. Zhou, D. Hou, K. Zhou, G. Li, Z. Tang, L. Li, S. Chen, Porous metallic MoO_2-supported MoS_2 nanosheets for enhanced electrocatalytic activity in the hydrogen evolution reaction, Nanoscale 7 (2015) 5203–5208.
[17] Y.J. Tang, M.R. Gao, C.H. Liu, S.L. Li, H.L. Jiang, Y.Q. Lan, M. Han, S.H. Yu, Porous molybdenum-based hybrid catalysts for highly efficient hydrogen evolution, Angew. Chem. Int. Ed. 54 (2015) 12928–12932.
[18] B. Zhang, Y. Xue, A. Jiang, Z. Xue, Z. Li, J. Hao, Ionic liquid as reaction medium for synthesis of hierarchically structured one-dimensional MoO_2 for efficient hydrogen evolution, ACS Appl. Mater. Interfaces 9 (2017) 7217–7223.
[19] M. Tian, F. Li, H. Hu, J. Ma, J. Jin, Nano-Cu-mediated multi-sites approach for growing ultrafine MoO_2 nanoparticles on PDDA-rGO as a robust hydrogen evolution electrocatalyst, ChemSusChem 12 (2018) 441–448.

[20] Z. Chen, G. Cao, L. Gan, H. Dai, N. Xu, M. Zang, H. Dai, H. Wu, P. Wang, Highly dispersed platinum on honeycomb-like NiO@Ni film as a synergistic electrocatalyst for the hydrogen evolution reaction, ACS Catal. 8 (2018) 8866–8872.

[21] J. Sun, Z. Wen, L. Han, Z. Chen, X. Lang, Q. Jiang, Nonprecious intermetallic Al_7Cu_4Ni nanocrystals seamlessly integrated in freestanding bimodal nanoporous copper for efficient hydrogen evolution catalysis, Adv. Funct. Mater. 28 (2018) 1706127.

[22] X. Wang, W. Li, D. Xiong, D.Y. Petrovykh, L. Liu, Bifunctional nickel phosphide nanocatalysts supported on carbon fiber paper for highly efficient and stable overall water splitting, Adv. Funct. Mater. 26 (2016) 4067–4077.

[23] Q. Zhang, P. Li, D. Zhou, Z. Chang, Y. Kuang, X. Sun, Superaerophobic ultrathin Ni-Mo alloy nanosheet array from in situ topotactic reduction for hydrogen evolution reaction, Small 13 (2017) 1701648.

[24] Y. Li, H. Yu, Z. Wang, S. Liu, Y. Xu, X. Li, L. Wang, H. Wang, Boron-doped silver nanosponges with enhanced performance towards electrocatalytic nitrogen reduction to ammonia, Chem. Commun. 55 (2019) 14745–14748.

[25] X. Peng, D. Chen, X. Yang, D. Wang, M. Li, C.-C. Tseng, R. Panneerselvam, X. Wang, W. Hu, J. Tian, Y. Zhao, Microwave-assisted synthesis of highly dispersed PtCu nanoparticles on three-dimensional nitrogen-doped graphene networks with remarkably enhanced methanol electrooxidation, ACS Appl. Mater. Interfaces 8 (2016) 33673–33680.

[26] D. Delgado, M. Minakshi, D.J. Kim, C. Kyeong W, Influence of the oxide content in the catalytic power of raney nickel in hydrogen generation, Anal. Lett. 50 (2017) 2386–2401.

[27] I. Herraiz-Cardona, C. González-Buch, C. Valero-Vidal, E. Ortega, V. Pérez-Herranz, Co-modification of Ni-based type Raney electrodeposits for hydrogen evolution reaction in alkaline media, J. Power Sources 240 (2013) 698–704.

[28] Y. Luo, L. Tang, U. Khan, Q. Yu, H.-M. Cheng, X. Zou, B. Liu, Morphology and surface chemistry engineering toward pH-universal catalysts for hydrogen evolution at high current density, Nat. Commun. 10 (2019) 269.

[29] L.J. Yang, Y.Q. Deng, X.F. Zhang, H. Liu, W.J. Zhou, $MoSe_2$ nanosheet/MoO_2 nanobelt/carbon nanotube membrane as flexible and multifunctional electrodes for full water splitting in acidic electrolyte, Nanoscale 10 (2018) 9268–9275.

[30] S.-L. Yang, H.-B. Yao, M.-R. Gao, S.-H. Yu, Monodisperse cubic pyrite NiS2 dodecahedrons and microspheres synthesized by a solvothermal process in a mixed solvent: thermal stability and magnetic properties, CrystEngComm 11 (2009) 1383–1390.

[31] P. Kumar, M. Singh, G.B. Reddy, Oxidation of core–shell MoO_2–MoS_2nanoflakes in different O_2ambience, Mater. Res. Express 4 (2017) 036405.

[32] J.H. Ku, Y.S. Jung, K.T. Lee, C.H. Kim, S.M. Oh, Thermoelectrochemically activated MoO_2 powder electrode for lithium secondary batteries, J. Electrochem. Soc. 156 (2009) A688–A693.

[33] G. Shaohui, L. Xuanhua, R. Xingang, Y. Lin, Z. Jinmeng, W. Bingqing, Optical and electrical enhancement of hydrogen evolution by MoS_2@MoO_3 core-shell nanowires with designed tunable plasmon resonance, Adv. Funct. Mater. 28 (2018) 1802567.

[34] R.D. Nikam, A.Y. Lu, P.A. Sonawane, U.R. Kumar, K. Yadav, L.J. Li, Y.T. Chen, Three-dimensional heterostructures of MoS_2 nanosheets on conducting MoO_2 as an efficient electrocatalyst to enhance hydrogen evolution reaction, ACS Appl. Mater. Interfaces 7 (2015) 23328–23335.

[35] H. Li, C. Mao, H. Shang, Z. Yang, Z. Ai, L. Zhang, New opportunities opened by nanosheets photocatalysts for efficient N2 fixation, Nanoscale 10 (2018) 15429–15435.

[36] L. An, Y. Li, M. Luo, J. Yin, Y.-Q. Zhao, C. Xu, F. Cheng, Y. Yang, P. Xi, S. Guo, Atomic-level coupled interfaces and lattice distortion on CuS/NiS_2 nanocrystals boost oxygen catalysis for flexible Zn-air batteries, Adv. Funct. Mater. 27 (2017) 1703779.

[37] H. Zhao, H. Zhang, G. Cui, Y. Dong, G. Wang, P. Jiang, X. Wu, N. Zhao, A photochemical synthesis route to typical transition metal sulfides as highly efficient cocatalyst for hydrogen evolution: from the case of NiS/g-C_3N_4, Appl. Catal., B 225 (2018) 284–290.

[38] C. Dahl-Petersen, M. Saric, M. Brorson, P.G. Moses, J. Rossmeisl, J.V. Lauritsen, S. Helveg, Topotactic growth of edge-terminated MoS_2 from MoO_2 nanocrystals, ACS Nano 12 (2018) 5351–5358.

[39] M. Qian, M. Xu, S. Zhou, J. Tian, T. Taylor Isimjan, Z. Shi, X. Yang, Template synthesis of two-dimensional ternary nickel-cobalt-nitrogen co-doped porous carbon film: promoting the conductivity and more active sites for oxygen reduction, J. Colloid Interface Sci. 564 (2019) 276–285.

[40] J. Guo, B. Wang, D. Yang, Z. Wan, P. Yan, J. Tian, T.T. Isimjan, X. Yang, Rugae-like Ni_2P-CoP nanoarrays as a bi-functional catalyst for hydrogen generation: $NaBH_4$ hydrolysis and water reduction, Appl. Catal. B: Environ. 265 (2019) 118584.

[41] E. Yavuz, K.V. Özdokur, İ. Çakar, S. Koçak, F.N. Ertaş, Electrochemical preparation, characterization of molybdenum-oxide/platinum binary catalysts and its application to oxygen reduction reaction in weakly acidic medium, Electrochim. Acta 151 (2015) 72–80.

[42] K.V. Özdokur, A.Y. Tatlı, B. Yılmaz, S. Koçak, F.N. Ertaş, Development of pulsed deposited manganese and molybdenum oxide surfaces decorated with platinum nanoparticles and their catalytic application for formaldehyde oxidation, Int. J. Hydrogen Energy 41 (2016) 5927–5933.

[43] S. Koçak, F.N. Ertaş, Z. Dursun, Electrochemical deposition and behavior of mixed-valent molybdenum oxide film at glassy carbon and ITO electrodes, Appl. Surf. Sci. 265 (2013) 205–213.

[44] L. Zhang, I.S. Amiinu, X. Ren, Z. Liu, G. Du, A.M. Asiri, B. Zheng, X. Sun, Surface modification of a NiS_2 nanoarray with $Ni(OH)_2$ toward superior water reduction electrocatalysis in alkaline media, Inorg. Chem. 56 (2017) 13651–13654.

[45] S. Meng, Y. Cui, H. Wang, X. Zheng, X. Fu, S. Chen, Noble metal-free 0D–1D NiS_x/CdS nanocomposites toward highly efficient photocatalytic contamination removal and hydrogen evolution under visible light, Dalton Trans. 47 (2018) 12671–12683.

[46] A.Y. Lu, X. Yang, C.C. Tseng, S. Min, S.H. Lin, C.L. Hsu, H. Li, H. Idriss, J.L. Kuo, K. W. Huang, L.J. Li, High-sulfur-vacancy amorphous molybdenum sulfide as a high current electrocatalyst in hydrogen evolution, Small 12 (2016) 5530–5537.

[47] Y. Shi, Y. Zhou, D.-R. Yang, W.-X. Xu, C. Wang, F.-B. Wang, J.-J. Xu, X.-H. Xia, H.-Y. Chen, Energy level engineering of MoS_2 by transition-metal doping for accelerating hydrogen evolution reaction, J. Am. Chem. Soc. 139 (2017) 15479–15485.

[48] S.-Q. Liu, H.-R. Wen, G. Ying, Y.-W. Zhu, X.-Z. Fu, R. Sun, C.-P. Wong, Amorphous $Ni(OH)_2$ encounter with crystalline CuS in hollow spheres: a mesoporous nano-shelled heterostructure for hydrogen evolution electrocatalysis, Nano Energy 44 (2018) 7–14.

[49] Y. Li, X. Tan, S. Chen, X. Bo, H. Ren, S. Smith, C. Zhao, Processable surface modification of nickel-heteroatom (N, S) bridge sites for promoted alkaline hydrogen evolution, Angew. Chem. Int. Ed. 58 (2019) 461–466.

[50] B. You, X. Liu, G. Hu, S. Gul, J. Yano, D.E. Jiang, Y. Sun, Universal surface engineering of transition metals for superior electrocatalytic hydrogen evolution in neutral water, J. Am. Chem. Soc. 139 (2017) 12283–12290.

[51] R. Subbaraman, D. Tripkovic, D. Strmcnik, K.-C. Chang, M. Uchimura, A.P. Paulikas, V. Stamenkovic, N.M. Markovic, Enhancing hydrogen evolution activity in water splitting by tailoring Li^+-$Ni(OH)_2$-Pt interfaces, Science 334 (2011) 1256–1260.

[52] H. Wang, Y. Wang, L. Tan, L. Fang, X. Yang, Z. Huang, J. Li, H. Zhang, Y. Wang, Component-controllable cobalt telluride nanoparticles encapsulated in nitrogen-doped carbon frameworks for efficient hydrogen evolution in alkaline conditions, Appl. Catal., B 244 (2019) 568–575.

[53] Y. Zheng, Y. Jiao, Y. Zhu, L.H. Li, Y. Han, Y. Chen, M. Jaroniec, S.Z. Qiao, High electrocatalytic hydrogen evolution activity of an anomalous ruthenium catalyst, J. Am. Chem. Soc. 138 (2016) 16174–16181.

[54] Y. Pan, K. Sun, Y. Lin, X. Cao, Y. Cheng, S. Liu, L. Zeng, W.-C. Cheong, D. Zhao, K. Wu, Z. Liu, Y. Liu, D. Wang, Q. Peng, C. Chen, Y. Li, Electronic structure and d-band center control engineering over M-doped CoP (M = Ni, Mn, Fe) hollow polyhedron frames for boosting hydrogen production, Nano Energy 56 (2019) 411–419.

[55] Z. Ji, C. Trickett, X. Pei, O.M. Yaghi, Linking molybdenum-sulfur clusters for electrocatalytic hydrogen evolution, J. Am. Chem. Soc. 42 (2018) 13618–13622.